Research Article

ADVANCED PHOTONICS

High-capacity free-space optical link in the midinfrared thermal atmospheric windows using unipolar quantum devices

Pierre Didier,[a,b,*,†] Hamza Dely,[c,†] Thomas Bonazzi,[c] Olivier Spitz,[a,d] Elie Awwad,[a] Étienne Rodriguez,[c] Angela Vasanelli,[c] Carlo Sirtori,[c] and Frédéric Grillot[a,e]

[a]Télécom Paris, Institut Polytechnique de Paris, LTCI, Palaiseau, France
[b]mirSense, Centre d'integration NanoInnov, Palaiseau France
[c]ENS, Université PSL, CNRS, Sorbonne Université, Université de Paris, Laboratoire de Physique de l'École Normale Supérieure, Paris, France
[d]University of Central Florida, CREOL, College of Optics and Photonics, Orlando, Florida, United States
[e]University of New Mexico, Center for High Technology Materials, Albuquerque, New Mexico, United States

Abstract. Free-space optical communication is a very promising alternative to fiber communication systems, in terms of ease of deployment and costs. Midinfrared light has several features of utter relevance for free-space applications: low absorption when propagating in the atmosphere even under adverse conditions, robustness of the wavefront during long-distance propagation, and absence of regulations and restrictions for this range of wavelengths. A proof-of-concept of high-speed transmission taking advantage of intersubband devices has recently been demonstrated, but this effort was limited by the short-distance optical path (up to 1 m). In this work, we study the possibility of building a long-range link using unipolar quantum optoelectronics. Two different detectors are used: an uncooled quantum cascade detector and a nitrogen-cooled quantum well-infrared photodetector. We evaluate the maximum data rate of our link in a back-to-back configuration before adding a Herriott cell to increase the length of the light path up to 31 m. By using pulse shaping, pre- and post-processing, we reach a record bitrate of 30 Gbit s^{-1} for both two-level (OOK) and four-level (PAM-4) modulation schemes for a 31-m propagation link and a bit error rate compatible with error-correction codes.

Keywords: free-space communication; Stark-effect external modulator; midinfrared photonics; intersubband technology; unipolar quantum devices.

Received Jun. 12, 2022; revised manuscript received Sep. 15, 2022; accepted for publication Oct. 7, 2022; published online Nov. 1, 2022.

© The Authors. Published by SPIE and CLP under a Creative Commons Attribution 4.0 International License. Distribution or reproduction of this work in whole or in part requires full attribution of the original publication, including its DOI.

[DOI: 10.1117/1.AP.4.5.056004]

1 Introduction

Since its adoption in the early 2000s, broadband communication has revolutionized our habits of learning, entertaining, and communicating, owing to continuous improvement in data-transfer speed. In some geographical areas, high-speed internet access is still hindered due to infrastructure issues: wired network expansion implies heavy civil engineering and very high costs. In the meantime, the development of novel midinfrared (MIR) sources like supercontinuum generation,[1] optical parametric oscillators (OPOs),[2] or cascade laser technology to replace bulky CO_2[3] and lead-salt lasers[4] has opened up promising prospects in fields such as spectroscopy,[5] medicine,[6] and free-space optics (FSO) communication. For the latter, wavelengths in the 8 to 14 μm transparency window of the atmosphere are more resistant to degraded atmospheric conditions,[7] including turbulence,[8] than their mid- (3 to 5 μm) and short-wave infrared counterparts. Semiconductor lasers in this range of the optical spectrum emerged with the realization of quantum cascade lasers (QCLs) in 1994,[9] which is now a technology mature enough for applications requiring reliable, powerful MIR sources at room temperature. QCL is a unipolar quantum device based on intersubband transitions with electrons relaxing within a few

*Address all correspondence to Pierre Didier, pierre.didier@telecom-paris.fr

†These authors contributed equally to this work.

picoseconds to their ground state.[10] This peculiarity should lead to electrical bandwidths of dozens of GHz[11] but, practically, local attenuation can worsen the frequency response of QCLs.[12] Direct modulation of these semiconductor lasers is thus lagging behind, with a 3-dB bandwidth in the range of 10 GHz for a configuration with an RF-launcher[13–16] while state-of-the-art detectors are much faster: MIR quantum-well-infrared photodetectors (QWIPs) able to detect frequencies above 100 GHz have been demonstrated for over 15 years.[17] The development efforts of such technology remain vivid: 70 GHz bandwidth QWIPs have been designed recently[18] as well as room-temperature quantum cascade detectors (QCDs) with a 3 dB bandwidth of 25 GHz.[19] Short-range proof-of-concept experiments with directly-modulated QCLs have shown little improvement in terms of data rate between the early days of intersubband technology[20] and the latest results achieving 6 Gbit s^{-1},[21] though most of the recent efforts[22–26] rely on fully integrated mercury-cadmium-telluride detectors with high responsivities but lower bandwidths.[27] Interestingly, a very recent result showed an 11-Gbit s^{-1} 9.6-μm transmission with a directly-modulated QCL associated with a QCD enhanced by computer-assisted processing.[28] External modulators are one of the key technologies to circumvent this bandwidth limitation, which may explain why QCL-based communications have not yet been widely adopted for long-haul free-space transmissions. Efforts exploring various technologies have introduced midinfrared modulators with bandwidths in the GHz range,[29–32] following seminal works with cryogenic lead-salt lasers and Ti-indiffused guided-wave interferometric modulators.[33] The first generation of unipolar modulators based on the transition between weak and strong light–matter coupling regimes demonstrated a 750-MHz bandwidth limited by drift transport velocity, with a 10% modulation depth.[34] Yet, communication systems require devices with a large signal-to-noise ratio (SNR) on top of a multi-GHz bandwidth, in order to accommodate bit-level separations, even if progress has recently been made to tackle strong background noise issues.[35]

In this article, we take the promising results recently obtained[36] with midinfrared Stark-effect[37] modulators one step further by extending the transmission range to 31 m with a Herriott cell. The high-power signal at the output of the modulator advocates for even longer distances of propagation that would require outside facilities and telescopes for beam shaping.[38] In addition, conventional signal pre- and post-processing is implemented in order to achieve a record transmission at a gross rate of 30 Gbit s^{-1} with 7% forward-error correction (FEC) overhead using OOK and 40 Gbit s^{-1} with 27% FEC using OOK and PAM-4 modulation schemes over 31 m, paving the way toward large-scale adoption in telecom applications. The main advantage of our method is that it can address any midinfrared wavelength and is not restricted by wavelength up- and downconversion, which remains a promising technique for communication below 4 μm.[39] In fact, these techniques benefit from the maturity of the devices at 1.5 μm in terms of bandwidth, power, and spectral purity to generate a transmitted midinfrared signal. However, the efficiency is still very low (order of mW) and bulky while power-consuming near-infrared pumps (order of multi-W) are needed.[40] Overall, this work shows the relevance of intersubband technology as a key building block of the midinfrared transmission (optical source, external modulator, and detector) and holds much promise as the size-reduction of the modulator is expected to drastically increase the maximum bandwidth, which is a trend already observed in intersubband detectors.[41]

2 Optical Setup

Our free-space communication setup is represented in Fig. 1. The optical source is a commercial 9-μm wavelength continuous

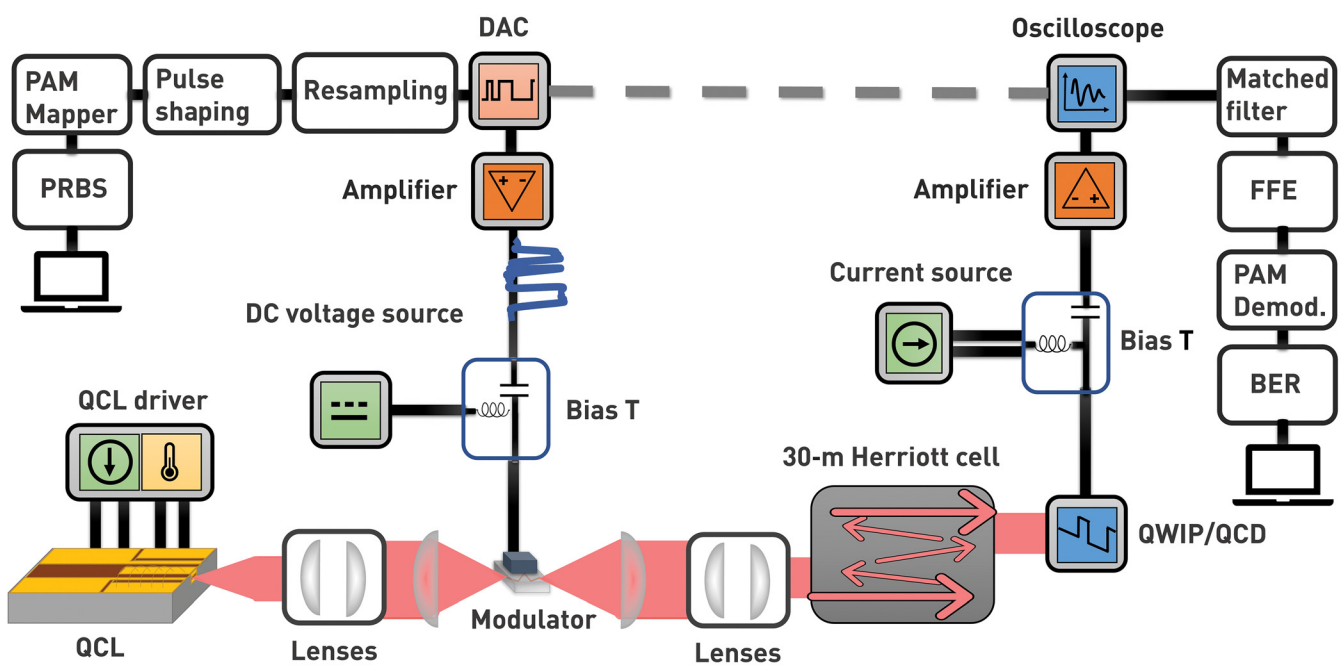

Fig. 1 Schematic of the full setup. A 9 μm wavelength CW QCL emits around 100 mW. The beam goes to an external modulator connected to DC and RF sources. The resulting signal passes through a 31-m Herriott cell before being collected on a high-speed detector and recorded with a fast oscilloscope.

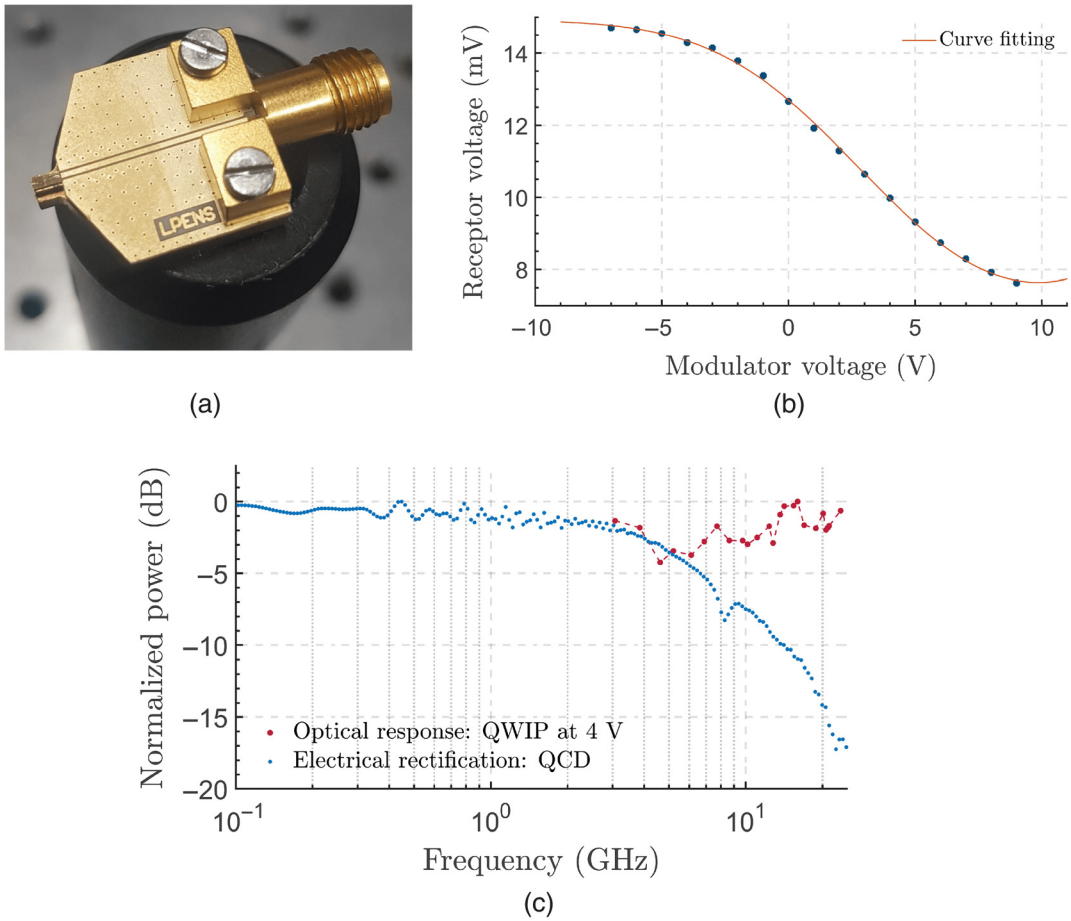

Fig. 2 (a) Picture of the connectorized external modulator on its mount with a coplanar waveguide. (b) Modulation depth estimated while measuring the signal voltage on the QCD when voltage pulses are applied on the modulator (blue dots). The measurements are well fitted with a Beer–Lambert law (solid curve). (c) QWIP biased at 4 V and showing a bandwidth >25 GHz with a heterodyne beating signal[42] (in red). We also display the electrical rectification of the QCD, showing a 3 dB bandwidth of 4.5 GHz (in blue).

wave (CW) QCL working at room temperature and emitting up to 97 mW of output power at room temperature. The beam emitted by the QCL is expanded with one telescope and focused using another telescope on a 50-μm × 50-μm external modulator [Fig. 2(a)]. The modulator is bonded to a custom coplanar waveguide and connected to a bias-tee with a 2.92-mm connector. DC bias is provided by an Agilent 33500B generator while the RF signal comes from a Socionext arbitrary waveform generator (AWG) that can provide 120 GS s^{-1}, with an analog 3-dB bandwidth of 30 GHz. The signal is amplified twice (differential 10 dB D837C and 25 dB 826H SHF amplifiers) to achieve 15-V peak-to-peak voltage required to drive the modulator. Such a high voltage is due to the strong impedance mismatch between the amplifier and the modulator. Tackling this issue to reduce the amplitude of the modulating signal would require a thorough characterization and optimization of the electrical circuit of the modulator to reduce parasitic capacitance and inductance. Two-thirds of the optical power is lost because of reflections on the modulator facets. The modulated midinfrared beam is either directly collected by a MIR high-speed detector or deviated through a 31-m Herriott cell before impinging on the detector. The received signal is acquired with a 33-GHz bandwidth high-speed oscilloscope (Tektronix DPO70000SX) and then processed off-line with Python and MATLAB scripts. Two detectors are used in this work: a passive, room-temperature QCD already presented in one of our previous works,[36] and a nitrogen-cooled 25-μm × 25-μm, mesa QWIP at 77 K with technology inspired by Ref. 17, showing in our case a bandwidth higher than 25 GHz, as shown in Fig. 2(c).

The Stark-effect-based external modulator is a 50-μm× 50-μm mesa designed for high-speed operation with quantum engineering preventing charge displacement in the heterostructure, thus avoiding speed throttling due to electronic transport. The 9-GHz bandwidth under RF probing (as depicted by the blue curve in Fig. 3) is mainly limited by its geometric capacitance. Bandwidth may be improved by reducing even further the size of the modulator at the cost of a more challenging optical alignment. To estimate its modulation depth, the modulator is excited with a few microsecond-long voltage pulses between 0 V and peak values V ranging from −7 to 9 V. The measurement procedure is detailed in Fig. S1 in the Supplementary Material. Figure 2(b) presents the peak voltage measured on

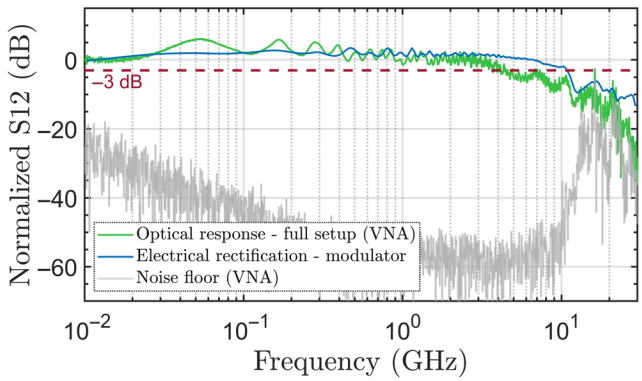

Fig. 3 Bandwidth measurements. Optical response of the full system (modulator, QWIP, and amplifiers) measured using a VNA and injecting a 5 dBm signal in the modulator (green curve). In blue, the rectified current from the modulator when injecting a 0 dBm input signal. The gray curve represents the noise obtained in the same configuration while the midinfrared beam is blocked.

the QCD (proportional to the peak intensity) for various pulse peak voltages applied to the modulator and a Beer–Lambert law fit,

$$V_D(V) = V_{D,0} \times \exp(-\alpha(V)), \tag{1}$$

where

$$\alpha(V) = \alpha_0 \times \exp\left(-\left(\frac{V - V_0}{\sigma}\right)^2\right) \tag{2}$$

is the voltage-dependent absorptivity of the modulator, with σ being the full width at half-maximum and V_0 the voltage at maximum absorption α_0 of the modulator. This leads to a 51.2% modulation depth between its maximum and minimum transmission, in good agreement with previous results obtained using another device made of the same material.[36] For high-voltage levels, the modulator exhibits nonlinear dynamics, which can be detrimental for the quality of the transmission by creating distortion; we thus avoid such conditions of operation in the following.

To get an overview of the capabilities of the system, several bandwidth metrics are measured (Fig. 3). First, we measure the electrical bandwidth of the modulator (blue curve) using electrical rectification, and that bandwidth is found to be 9 GHz. This technique consists in measuring the DC current generated by the nonlinear current-voltage characteristic under sinusoidal excitation.[43] Then, we use a vector network analyzer (VNA) in order to characterize the frequency response of the full system (modulator, QWIP, and amplifiers) by injecting a 5 dBm electrical signal. This results in the green curve of Fig. 3, while the gray one gives the electrical noise of the exact same system when blocking the beam. Despite a high-level noise above 13 GHz, the signal-to-noise ratio in the 0.1- to 10-GHz range is above 40 dB. The QCL is driven 1.5 times above its threshold current (280 mA). Since the relative intensity noise (RIN) decreases with bias current,[44] we assume that the RIN is negligible compared to electrical noise coming from the amplifiers. Compared with our previous setup,[36] using a smaller modulator improves the bandwidth by a factor of two and allows for reaching 3-dB bandwidth of 4.5 GHz.

3 Data Transmission Using External Modulator

In this experiment, on–off keying (OOK) and four-level pulse amplitude modulation (PAM-4) are used to transmit data using pseudorandom binary sequences (PRBSs), which are either 2^7- or 2^{15}-bit-long patterns. We bias the modulator at a DC value of 1.1 V to work in its linear regime and to reduce distortion as much as possible. We perform measurements for back-to-back (B2B) transmission (i.e., roughly 2-m propagation), and for 31-m propagation transmission using a commercial Herriott cell (Thorlabs HC30L/M-M02) that is inserted in the path of the midinfrared beam. This cell is a two-mirror cavity with a small shifted aperture on each of the mirrors to make the beam bounce back and forth 80 times before exiting. This process adds extra optical losses in the system, but this is limited to 3 dB in our case because the mirrors have a specific coating allowing for a reflectivity higher than 99% at the wavelength of interest. An extra telescope is needed right before the multipass cell to shape the beam and ensure good beam quality at the output of the cell. The transmitted signal is collected by either the QCD or the QWIP detector. In order to evaluate the quality of the transmission, we derive the ratio between the errors in the received data and the total number of bits sent, commonly referred as the bit error rate (BER). The BER is evaluated for the entire acquired sequences that contain ten million samples sampled at 100 GS s^{-1}. If the BER is below a given threshold, error-correction algorithms can be implemented to correct any remaining errors. Here, we assume that a forward error correction (FEC) code is used to correct the erroneous bits and subsequently leads to an error-free transmission (i.e., orders of magnitude lower BER than presented here) after FEC decoding. However, FEC implies a rate reduction due to the introduction of redundancy bits in data frames. For a maximum pre-FEC BER of 4%, an FEC code leads to a 27% bit overhead and hard-decision (HD) decoding is assumed to be used to achieve an error-free communication, whereas a maximum pre-FEC BER of 0.38% only requires 7% overhead.[45] In our case, the optimal results in terms of data rate are obtained for 27% HD-FEC, but a larger overhead introduces more latency because it requires a more complex decoding. For every experiment, we present the gross data rates in the text and the corresponding net bit rates in Table 1 after subtracting the FEC (7% or 27%) and the pilot sequences (5%) overheads. In the following, we will present the eye diagrams of the received

Table 1 Summary of results in terms of net data rates by taking into consideration overhead of the FEC (HD-FEC 7% and 27%) and the pilot sequence (5%) for equalized signal.

	Net data rates (Gbit/s)			
	QCD		QWIP	
	OOK	PAM4	OOK	PAM4
Back to back (2 m)	*21* & **26**	*9* & **8**	*26* & **30**	*21* & **33**
Herriott cell (31 m)	*12.5* & **18**	—	*26* & **30**	*21* & **30**

Italic values: 7% HD-FEC overhead. Bold values: 27% HD-FEC overhead.

signals in order to evaluate the quality of the transmission for several configurations. An eye diagram is a graphical display where the signal is repetitively overlapped on a time interval corresponding to an integer multiple of the bit time length. This tool allows a qualitative analysis of the transmission performance, as an open eye is equivalent to a low error rate.

We first show the results in B2B in Fig. 4(a). We achieve a rate of 16 Gbit s^{-1} without any further processing and with a BER of 0.38% using a cooled QWIP. However, with the QCD receiver, we were only able to reach a BER of 4% at 16 Gbit s^{-1} because of the noisy environment added by the amplifier, the modulator, and the laser source. Later, we perform a transmission experiment over a distance of 31 m by using the Herriott cell. With the QWIP receiver, we are able to transmit at 16 Gbit s^{-1} with a BER of 3.7% without further digital processing. With the QCD receiver, the lower responsivity and narrower 3-dB bandwidth (around 4.5 GHz) were detrimental for the transmission; consequently, we did not achieve a transmission with a BER below 4%. Indeed, the electrical signal at the output of the QCD is low (around 100 μV peak-to-peak) leading to the use of a high-gain 40-dB amplifier, which adds extra distortion and affects the quality of the transmission.

3.1 Feed-Forward Equalization

Digital equalization is a key step in order to improve dramatically the maximum data rates by compensating the systematic distortions of the channel and minimizing intersymbol interference.[46] We apply a fractional-spaced feed-forward equalization (FFE) scheme on the received signal sampled at a rate of four samples per symbol to equalize the received signal. We first learn the coefficients of the FFE filter using a gradient descent (steepest descent) algorithm with a convergence parameter μ that controls the speed and the accuracy of the learning step. Then, we equalize the received signal using the learned filter for which we define the number of coefficients as n_{tap}. The two parameters, μ and n_{tap}, are evaluated to optimize the efficiency of the quality transmission. We keep the n_{tap} value below 400 samples (or equivalently 100 symbols) in order to keep a low latency. A smaller value of μ allows for a more accurate, albeit slower, estimation of the channel distortions while a higher value allows for a fast, however less accurate, estimation. Figure 5 demonstrates the effect of FFE on a B2B 30-Gbit s^{-1} transmission performed with the QWIP. The BER without equalization is as high as 7%, so it is impossible to recover error-free data without equalization. By using an FFE with $n_{\text{tap}} = 391$ and $\mu = 1 \times 10^{-5}$, the BER drops from 7% to 0.1%, making the 30-Gbit s^{-1} transmission error-free when taking into account a subsequent 7% HD-FEC overhead. We are able to reach 40 Gbit s^{-1} with a 2^{15} bit-long PRBS for a B2B transmission with 27% HD-FEC overhead. This bit rate is even pushed to 48 Gbit s^{-1} in the case of a 2^7 bit-long PRBS and 27% HD-FEC overhead. In Fig. 5(b), one can see that the transmission quality is much improved by the implementation of equalization. With the QCD transmission, the maximum data rate is 24 Gbit s^{-1} for a BER $< 0.4\%$ and a sequence length of 2^7 as shown in Fig. 5(c).

3.2 31-m Transmission Using Herriott Cell

We now examine the feasibility of a high-quality transmission over a few dozen of meters. A 30-Gbit s^{-1} transmission using OOK with a sequence length of 2^{15} through the Herriott cell has been achieved with a QWIP, as plotted in Fig. 6. The red dots of Fig. 6(d) show the BER before equalization, while the blue ones are the BER after equalization, demonstrating an enhancement by more than one order of magnitude up to 30 Gbit s^{-1}. When the same experiment was conducted with the QCD for a 2^7-bit long sequence, the maximum data rate we could achieve was 14 Gbit s^{-1} at BER $= 0.21\%$ as shown in Fig. 6(a), limited by electrical noise coming from the high-gain amplifiers already mentioned.

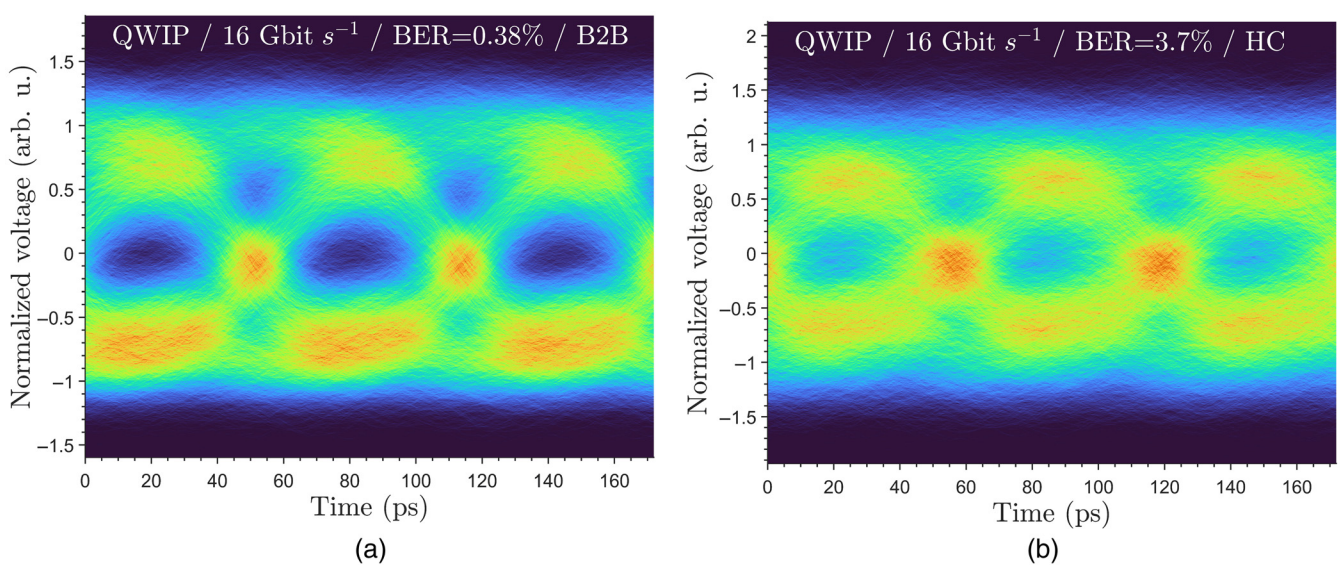

Fig. 4 Eye diagrams of transmission without processing for two different data rates using a QWIP. The figure shows the normalized voltage as a function of time: (a) 16 Gbit s^{-1} for a B2B transmission for a BER $<0.38\%$ and (b) 16 Gbit s^{-1} through a 31-m Herriott cell for a BER $<4\%$.

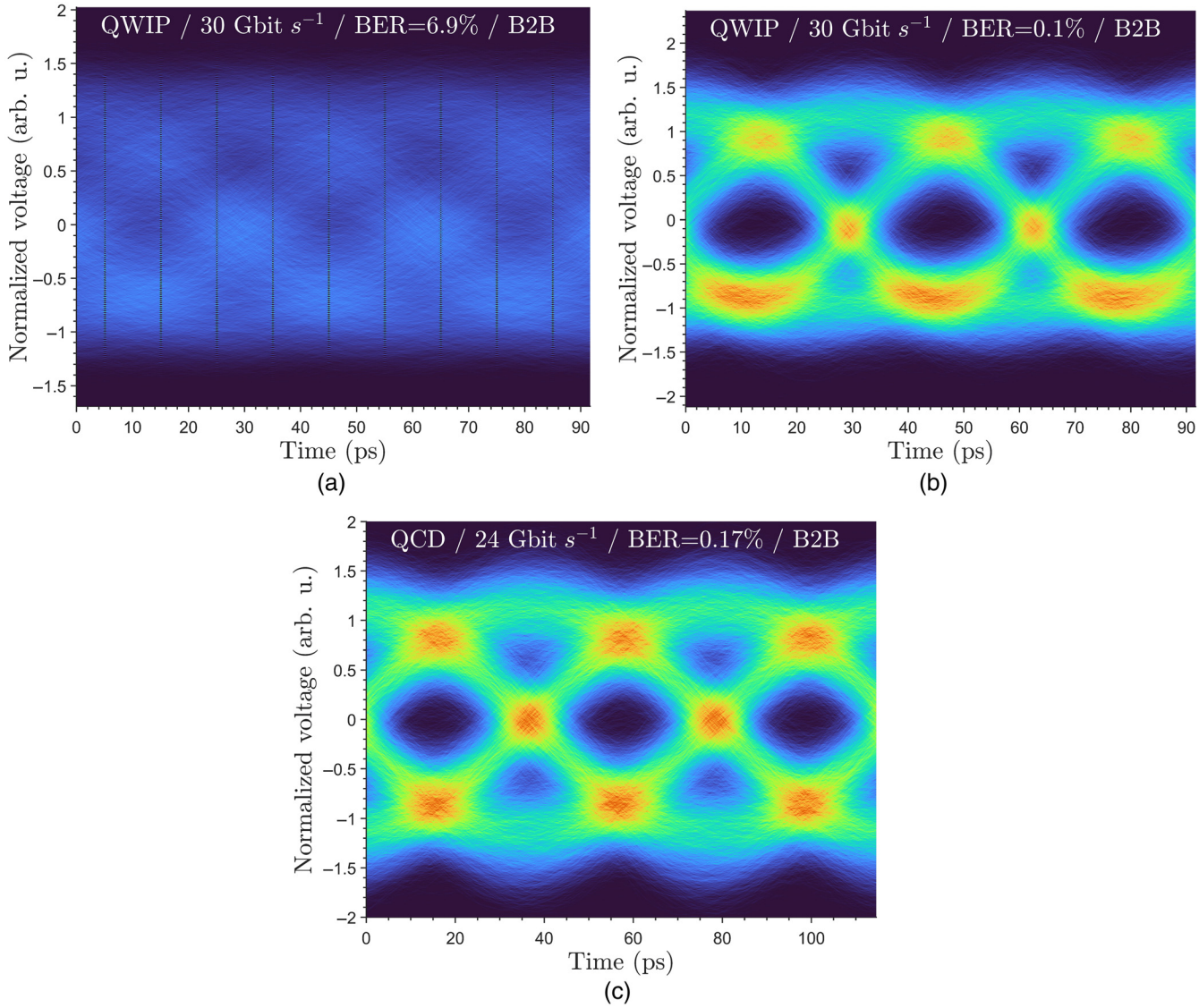

Fig. 5 Comparison of the two eye diagrams (a) without and (b) with FFE equalization ($n_{\text{tap}} = 391$ and $\mu = 1 \times 10^{-5}$) at 30 Gbit s^{-1} with a 2^{15}-bit long PRBS in B2B configuration. FFE corrects systematic channel defects and intersymbol interference, hence opening the eye. (c) Eye diagrams for back-to-back transmission after equalization for a 2^7-bit long PRBS at 24 Gbit s^{-1}.

3.3 Four-Level Transmission (PAM-4)

To further increase the bit rate using the same symbol rates, switching to higher-order modulation formats, such as PAM-4, is relevant. Further, in some scenarios below, we apply a digital pulse shaping root-raised-cosine (RRC) filter in order to reduce the spectral occupation of the transmitted signal. In these cases, the occupied bandwidth around the optical carrier is $B = (1 + \rho)R_s$ where ρ is the roll-off factor of the filter and R_s is the symbol rate. If ρ is close to 1, the bandwidth occupancy is maximum, typically twice the value of the symbol rate. Reducing ρ allows limiting the bandwidth occupancy. By applying pulse shaping with $\rho = 0.5$ at the transmitter side and FFE equalization at the receiver side, we are able to reach 70 Gbit s^{-1} with a 2^7-bit long PRBS and a resulting BER of 3.6% in the B2B configuration. An error-free transmission is impossible to achieve in the same conditions without pulse shaping nor FFE equalization. This result probably overestimates the capacity of our link because of the reduced sequence length. More realistically, we achieve 40 Gbit s^{-1} with a 2^{15} bit-long sequence and a resulting BER of <4%, both in the B2B configuration and in the 31-m link, as shown in Fig. 7.

4 Link Budget for Free-Space Transmission

During its propagation, the beam suffers from degradation due to the interaction with the medium, which is in our case the atmosphere. It may come from absorption by gas molecules like carbon dioxide, scattering, or wavefront deformation induced by turbulence. Neglecting wandering and the effect of turbulence in a first approach, losses caused by the propagation of our Gaussian laser beam at 9 μm can be written as[47,48]

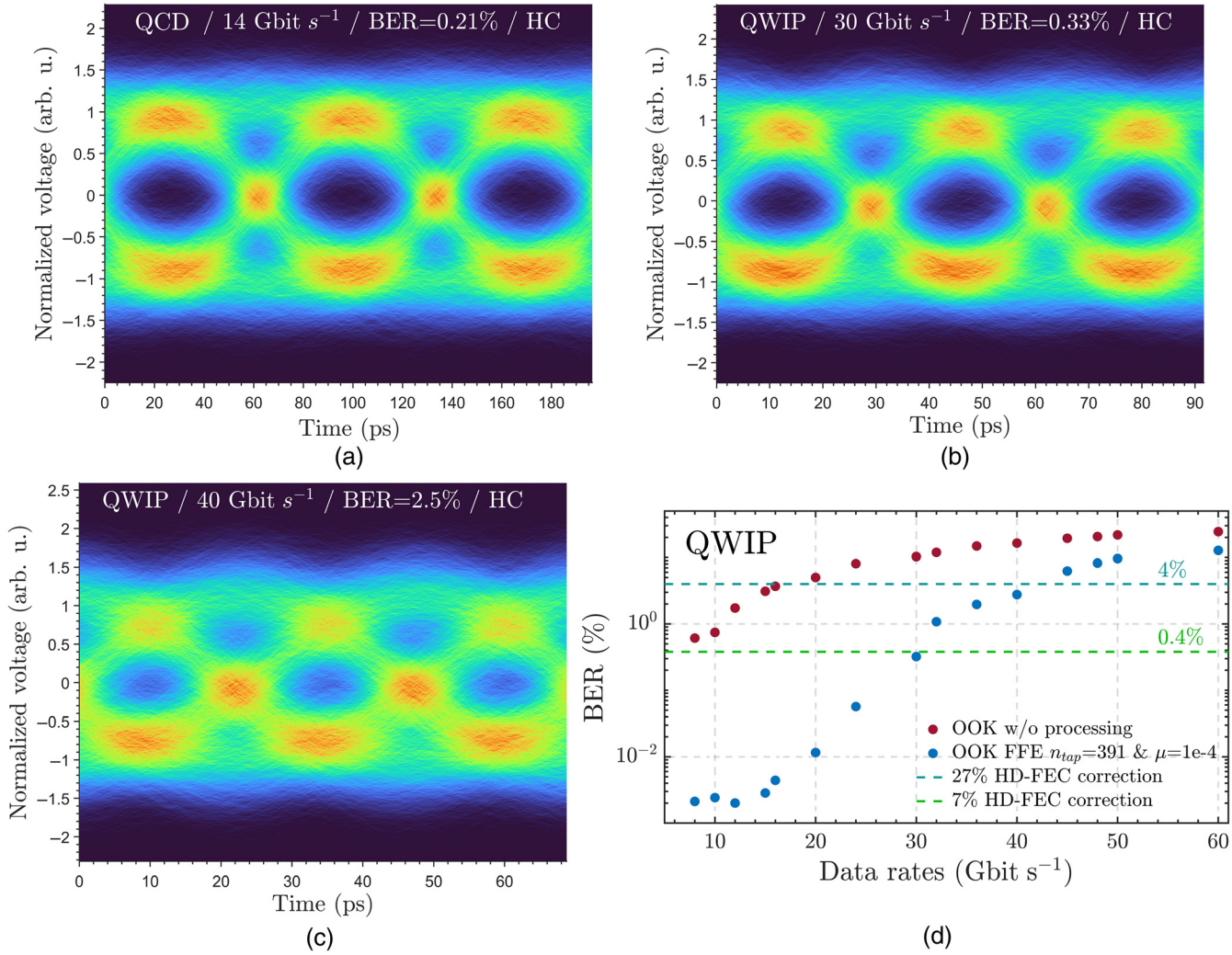

Fig. 6 Eye diagrams of the transmission through a 31-m Herriott cell for three different data rates and a sequence length of 2^7 for the QCD and 2^{15} for the QWIP. (a) QCD: 14 Gbit s^{-1} for a BER = 0.21%. (b) QWIP: 30 Gbit s^{-1} for a BER = 0.33%. (c) QWIP: 40 Gbit s^{-1} for a BER = 2.5%. (d) Evolution of the BER (equalized and nonequalized) with respect to the baudrate for the QWIP transmission. The dashed lines recall BER limits for 7% HD-FEC (green) and 27% HD-FEC (cyan).

$$P_R = P_T \frac{D_{Rx}^2}{(D_{Tx} + \theta_{\text{div}} L)^2} e^{-\gamma(\lambda)L}, \tag{3}$$

where P_R is the power at the reception, P_T is the emitting power, D_{Rx} and D_{Tx} are the diameters of the receiver and the transmitter, respectively, L is the propagation distance, and the beam divergence can be expressed as $\theta_{\text{div}} = \frac{\lambda}{\pi\omega_0}$ far from the origin. Here, $\gamma(\lambda)$ represents the relative attenuation caused by atmospherics losses and is written as $\gamma(\lambda) = \alpha_m(\lambda) + \alpha_a(\lambda) + \beta_m(\lambda) + \beta_a(\lambda)$, where α_m, α_a represent the absorption coefficients of the molecule and of the aerosol and β_m, β_a their respective diffusion coefficients. Using Eq. (4) in the Appendix with an $L = 1$ km FSO link in different weather conditions and basic optics with a 10-cm aperture (transmitter and receiver), we calculate overall attenuation which can be found in Table 2. For our externally modulated beam at 9 μm, we calculate an absorption and scattering attenuation of -0.2 dB km^{-1} while the divergence of the laser beam induces a -8.6 dB km^{-1} attenuation. Note that these values could be easily decreased by using more advanced optics. It leads to total losses of around -8.8 dB in this configuration. Assuming 30 mW of output power, we retrieve around 4 mW, which is sufficient to detect a signal and receive the message. In a situation where the visibility goes down to $V = 1$ km, which corresponds to mist visibility, attenuation due to scattering jumps to -3.3 dB km^{-1}, which remains small compared with equivalent scattering at $\lambda = 1.5$ μm (-9.3 dB km^{-1}) and at $\lambda = 4$ μm (-5.4 dB km^{-1}). In addition, if there is a particular weather condition like rain, snow, or large dust, we have to take into account the geometric scattering for which the absorption coefficients can be approximated with the formula expressed in the appendices. The drawback at longer wavelengths comes from the optical element's size, which needs to be increased accordingly to cope with the effect of divergence.

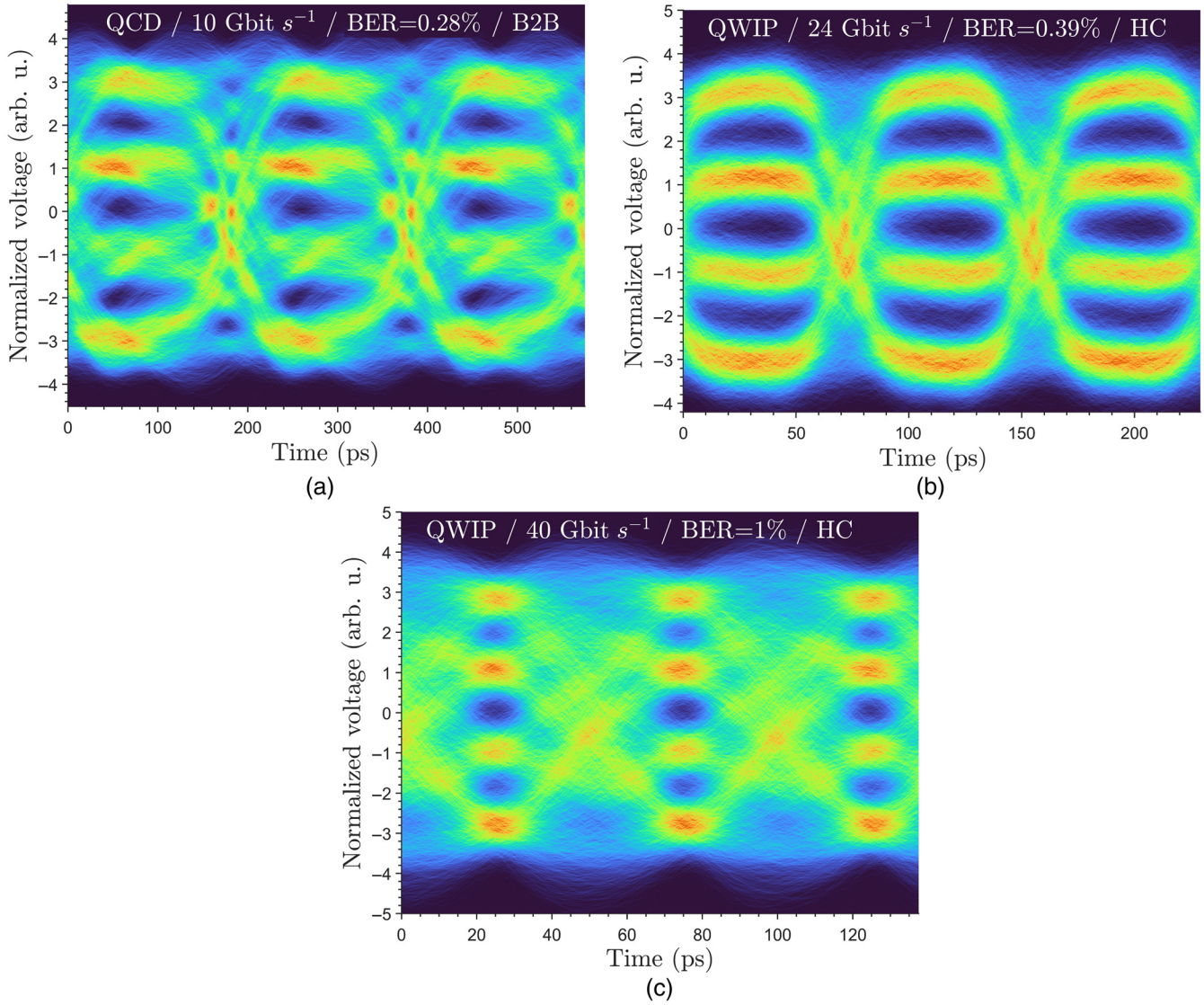

Fig. 7 (a) Eye diagram of a B2B equalized 2^7 PRBS transmission for the QCD with parameters ($n_{\text{tap}} = 391$, $\mu = 1 \times 10^{-4}$ with no RRC shaping) at 10 Gbit s^{-1}. (b) Eye diagram of a 31-m equalized 2^7 PRBS transmission for the QWIP with parameters ($n_{\text{tap}} = 391$, $\mu = 1 \times 10^{-5}$ with no RRC shaping) at 24 Gbit s^{-1}. (c) Eye diagram of a 31-m equalized 2^7 PRBS transmission for the QWIP with parameters ($n_{\text{tap}} = 391$, $\mu = 1 \times 10^{-5}$ with an RRC shaping with $\rho = 0.5$) at 40 Gbit s^{-1}.

Table 2 Beam attenuation caused by the Mie scattering inspired by the table of Trichili et al.[48]

	Attenuation (dB/km)		
Visibility (km)	1550 nm	4000 nm	9000 nm
20 (Clear)	0.2	0.06	0.02
5 (Haze)	1.2	0.47	0.2
2 (Mist)	4	2	1.1
1 (Fog)	9.3	5.4	3.3

5 Conclusion

We demonstrated a 31-m long high bitrate data transmission in the 8 μm to 14 μm thermal atmospheric window at a gross rate of 30 Gbit s^{-1}, with a BER below 0.4% related to 7% HD-FEC using a full set of intersubband quantum devices. This feat was made possible by pre- and post-processing algorithms. For some cases, we shaped the PAM-4 signal with an RRC routine before injecting it into the modulator. In addition, the received signal detected by our high-speed QWIP was equalized by a feed-forward equalization algorithm. Full room-temperature link up to 16 Gbit s^{-1} with a BER below 0.4% and 7% HD-FEC was also demonstrated with the exact same distance on our

QCD, limited by its low responsivity and high electronic amplifier noise. For a shorter distance transmission (i.e., B2B configuration), we achieved gross rates of 30 Gbit s^{-1} with the QWIP and 24 Gbit s^{-1} with the QCD, corresponding to a BER below 0.4% and 7% HD-FEC. This work is a key step toward the realization of a real-field midinfrared FSO system as it is, to the best of our knowledge, the first high throughput transmission setup on such a distance in this wavelength domain. In order to create a long-haul FSO link in the midinfrared, we need to build an adaptive optics system to account for other phenomena that can degrade the transmission. This platform has to be able to compensate for the effects of turbulence on the wavefront,[49] to avoid pointing errors, and to maximize the received power. Also, our room-temperature detectors are not good enough to target either larger link capacity or range. Nonetheless, this bottleneck can be easily overcome using an actual state-of-the-art MIR detector and yield far better bitrates at room temperature. Furthermore, the beam-shaping method used here for long-range transmission is straightforward and limited to our use-case with the multipass cell. It can be improved with cutting-edge adaptive optics techniques. Likewise, the link capacity could be increased by improving the electronic design on several aspects such as proper impedance matching networks to avoid detrimental frequency behaviors with the amplifiers. A new generation of faster patch antenna-based modulators with reduced capacitance would also bring substantial enhancements with a system bandwidth beyond 50 GHz. Considering ongoing efforts to design fully integrated systems made of intersubband devices, unipolar quantum optoelectronics could bring fast, reliable, and easy-to-deploy optical MIR links within reach in the coming years and be coupled with the recent findings about quantum cascade laser photonic chaos[50] to lead to private communication systems resistant to adverse weather conditions.

6 Appendix

At this wavelength, the major cause of diffusion is the Mie and the geometric scattering. Mie's theory describes elastic scattering light in the direction of propagation caused by particles with a similar or larger diameter than the wavelength. It is mainly caused by fog and haze. We have $\beta_{\mathrm{al}}(\lambda)$, according to the empirical Kim model,[47,51]

$$\beta_{\mathrm{al}}(\lambda) = \frac{3.91}{V}\left(\frac{\lambda}{\lambda_0}\right)^{-q}, \tag{4}$$

where λ_0 is the reference wavelength, V is the visibility range, q is the size distribution of the scattering particles, $q = 0$ for $V < 0.5$ km, $q = V - 0.5$ for $0.5\ \mathrm{km} < V < 1$ km, $q = 0.58V^{1/3}$ for $1\ \mathrm{km} < V < 6$ km, $q = 1.3$ for $6\ \mathrm{km} < V < 50$ km and $q = 1.6$ for $V > 50$ km.

The signal endures attenuation due to the presence of large particles like snow, rain, or fog. This is geometric scattering. We describe the different values caused by geometric scattering $\gamma\ (\mathrm{dB.km}^{-1})$.[52]

- Rain: $\gamma_{\mathrm{rain}} = K_R \cdot K^{\alpha_R}$, where R is the precipitation intensity, K_R and α_R are empirical values that depend on raindrop size and rain temperature that can be found in the literature.
- Snow: $\gamma_{\mathrm{snow}} = a_S \cdot S^{b_s}$, where S is the snowfall rate (mm/h), and a_S and b_S are snow parameters whose values change if the snow is wet or dry. We have $a_S = 0.000102\lambda + 3.79$ and $b_S = 0.72$ for wet snow and $a_S = 0.0000542\lambda + 5.50$, $b_S = 1.38$ for dry snow.
- Dust: $\gamma_{\mathrm{dust}} = K_d \cdot B^{b_d}$, where K_d and b_d are also empirical values that can be chosen as 52 and -1.05, respectively.[53]

Acknowledgments

The authors acknowledge the financial support of the Direction Générale de l'Armement (DGA), the ENS-Thales Chair, ANR project LIGNEDEMIR (ANR-18CE09-0035), FETOpen 2018–2020 Horizon 2020 projects cFLOW (Grant No. 828893) and QOMBS (Grant No. 820419) and CNRS Renatech network. The authors also would like to thank Jean-Christophe Cousin (Télécom Paris) and Adel Bousseksou (C2N) for lending the Vector Network Analyzer and for providing the liquid nitrogen, respectively. The authors declare no conflicts of interest.

Code, Data, and Materials Availability

Data underlying the results presented in this paper are not publicly available at this time but may be obtained from the authors upon reasonable request.

References

1. M. Montesinos-Ballester et al., "On-chip mid-infrared supercontinuum generation from 3 to 13 μm wavelength," *ACS Photonics* **7**(12), 3423–3429 (2020).
2. B. Cole et al., "Compact and efficient mid-IR OPO source pumped by a passively Q-switched Tm: YAP laser," *Opt. Lett.* **43**(5), 1099–1102 (2018).
3. N. Sobolev and V. V. Sokovikov, "CO_2 lasers," *Sov. Phys. Usp.* **10**(2), 153 (1967).
4. M. Tacke, "New developments and applications of tunable IR lead salt lasers," *Infrared Phys. Technol.* **36**(1), 447–463 (1995).
5. L. Zhang et al., "Applications of absorption spectroscopy using quantum cascade lasers," *Appl. Spectrosc.* **68**(10), 1095–1107 (2014).
6. T. H. Risby and F. K. Tittel, "Current status of midinfrared quantum and interband cascade lasers for clinical breath analysis," *Opt. Eng.* **49**(11), 111123 (2010).
7. P. Corrigan et al., "Quantum cascade lasers and the Kruse model in free space optical communication," *Opt. Express* **17**(6), 4355–4359 (2009).
8. J. J. Liu et al., "Mid and long-wave infrared free-space optical communication," *Proc. SPIE* **11133**, 1113302 (2019).
9. J. Faist et al., "Quantum cascade laser," *Science* **264**(5158), 553–556 (1994).
10. R. Ferreira and G. Bastard, "Evaluation of some scattering times for electrons in unbiased and biased single- and multiple-quantum-well structures," *Phys. Rev. B* **40**, 1074–1086 (1989).
11. B. Meng and Q. J. Wang, "Theoretical investigation of injection-locked high modulation bandwidth quantum cascade lasers," *Opt. Express* **20**(2), 1450–1464 (2012).
12. A. Calvar.et al., "High frequency modulation of mid-infrared quantum cascade lasers embedded into microstrip line," *Appl. Phys. Lett.* **102**(18), 181114 (2013).
13. B. Hinkov et al., "RF-modulation of mid-infrared distributed feedback quantum cascade lasers," *Opt. Express* **24**(4), 3294–3312 (2016).
14. A. Mottaghizadeh et al., "Ultra-fast modulation of mid infrared buried heterostructure quantum cascade lasers," in *42nd Int. Conf. Infrared, Millimeter, and Terahertz Waves (IRMMW-THz)*, IEEE, pp. 1–2 (2017).
15. Y. Zhou et al., "High-speed operation of single-mode tunable quantum cascade laser based on ultra-short resonant cavity," *AIP Adv.* **11**(1), 015325 (2021).
16. F. Kapsalidis et al., "Mid-infrared quantum cascade laser frequency combs with a microstrip-like line waveguide geometry," *Appl. Phys. Lett.* **118**(7), 071101 (2021).

17. P. Grant et al., "Room-temperature heterodyne detection up to 110 GHz with a quantum-well infrared photodetector," *IEEE Photonics Technol. Lett.* **18**(21), 2218–2220 (2006).
18. M. Hakl et al., "Ultrafast quantum-well photodetectors operating at 10 μm with a flat frequency response up to 70 GHz at room temperature," *ACS Photonics* **8**(2), 464–471 (2021).
19. G. Quinchard et al., "High speed, antenna-enhanced 10.3 μm quantum cascade detector," *Appl. Phys. Lett.* **120**(9), 091108 (2022).
20. R. Martini et al., "High-speed digital data transmission using mid-infrared quantum cascade lasers," *Electron. Lett.* **37**(21), 1290–1292 (2001).
21. X. Pang et al., "Up to 6 Gbps mid-infrared free-space transmission with a directly modulated quantum cascade laser," in *Eur. Conf. Opt. Commun. (ECOC)*, IEEE, pp. 1–4 (2021).
22. C. Liu et al., "Free-space communication based on quantum cascade laser," *J. Semicond.* **36**(9), 094009 (2015).
23. X. Pang et al., "Free-space communications enabled by quantum cascade lasers," *Phys. Status Solidi A* **218**(3), 2000407 (2021).
24. J. Mikołajczyk, "A comparison study of data link with medium-wavelength infrared pulsed and CW quantum cascade lasers," *Photonics* **8**(6), 203 (2021).
25. O. Spitz et al., "Multi-Gb/s free-space communication with energy-efficient room-temperature quantum cascade laser emitting at 8.1 μm," in *IEEE Photonics Conf. (IPC)*, IEEE, pp. 1–2 (2021).
26. O. Spitz et al., "Free-space communication with directly modulated mid-infrared quantum cascade devices," *IEEE J. Sel. Top. Quantum Electron.* **28**(1), 1200109 (2022).
27. B. Chen, Y. Chen, and Z. Deng, "Recent advances in high speed photodetectors for eSWIR/MWIR/LWIR applications," *Photonics* **8**(1), 14 (2021).
28. X. Pang et al., "11 Gb/s LWIR FSO transmission at 9.6 μm using a directly-modulated quantum cascade laser and an uncooled quantum cascade detector," in *Opt. Fiber Commun. Conf. and Exhibition (OFC)*, IEEE, pp. 1–3 (2022).
29. Y. Yao et al., "Electrically tunable metasurface perfect absorbers for ultrathin mid-infrared optical modulators," *Nano Lett.* **14**(11), 6526–6532 (2014).
30. B. Zeng et al., "Hybrid graphene metasurfaces for high-speed mid-infrared light modulation and single-pixel imaging," *Light: Sci. Appl.* **7**(1), 51 (2018).
31. G. Liang et al., "Mid-infrared photonics and optoelectronics in 2D materials," *Mater. Today* **51**, 294–316 (2021).
32. M. Montesinos-Ballester et al., "Mid-infrared integrated electro-optic modulator operating up to 225 MHz between 6.4 and 10.7 m wavelength," *ACS Photonics* **9**(1), 249–255 (2022).
33. R. Becker, R. Rediker, and T. Lind, "Wide-bandwidth guided-wave electro-optic intensity modulator at $\lambda = 3.39$ μm," *Appl. Phys. Lett.* **46**(9), 809–811 (1985).
34. S. Pirotta et al., "Fast amplitude modulation up to 1.5 GHz of mid-IR free-space beams at room-temperature," *Nat. Commun.* **12**, 799 (2021).
35. B. Crockett et al., "Optical signal denoising through temporal passive amplification," *Optica* **9**(1), 130–138 (2022).
36. H. Dely et al., "10 Gbit s–1 free space data transmission at 9 μm wavelength with unipolar quantum optoelectronics," *Laser Photonics Rev.* **16**(2), 2100414 (2022).
37. F. Capasso, C. Sirtori, and A. Y. Cho, "Coupled quantum well semiconductors with giant electric field tunable nonlinear optical properties in the infrared," *IEEE J. Quantum Electron.* **30**(5), 1313–1326 (1994).
38. M. Vorontsov et al., "Deep turbulence effects compensation experiments with a cascaded adaptive optics system using a 3.63 m telescope," *Appl. Opt.* **48**(1), A47–A57 (2009).
39. K. Zou et al., "Demonstration of free-space 300-Gbit/s QPSK communications using both wavelength-and mode-division-multiplexing in the mid-IR," in *Opt. Fiber Commun. Conf. and Exhibition (OFC)*, IEEE, pp. 1–3 (2021).
40. Q. Hao et al., "Mid-infrared transmitter and receiver modules for free-space optical communication," *Appl. Opt.* **56**(8), 2260–2264 (2017).
41. J. Hillbrand et al., "High-speed quantum cascade detector characterized with a mid-infrared femtosecond oscillator," *Opt. Express* **29**(4), 5774–5781 (2021).
42. D. Palaferri et al., "Room-temperature nine-μm-wavelength photodetectors and GHz-frequency heterodyne receivers," *Nature* **556**(7699), 85–88 (2018).
43. H. Liu et al., "High-frequency quantum-well infrared photodetectors measured by microwave-rectification technique," *IEEE J. Quantum Electron.* **32**(6), 1024–1028 (1996).
44. T. Gensty, "Intensity noise properties of quantum cascade lasers," *Opt. Express* **13**(6), 2032–2039 (2005).
45. O. Ozolins et al., "100 Gbaud PAM4 link without EDFA and post-equalization for optical interconnects," in *45th Eur. Conf. Opt. Commun. (ECOC 2019)*, IET, pp. 1–4 (2019).
46. J. G. Proakis and M. Salehi, *Digital Communications*, Vol. **4**, McGraw-Hill, New York (2001).
47. I. I. Kim, B. McArthur, and E. J. Korevaar, "Comparison of laser beam propagation at 785 nm and 1550 nm in fog and haze for optical wireless communications," *Proc. SPIE* **4214**, 26–37 (2001).
48. A. Trichili et al., "Roadmap to free space optics," *J. Opt. Soc. Am. B* **37**(11), A184–A201 (2020).
49. Y. Ren et al., "Adaptive-optics-based simultaneous pre-and post-turbulence compensation of multiple orbital-angular-momentum beams in a bidirectional free-space optical link," *Optica* **1**(6), 376–382 (2014).
50. O. Spitz et al., "Private communication with quantum cascade laser photonic chaos," *Nat. Commun.* **12**, 3327 (2021).
51. H. Kaushal, V. Jain, and S. Kar, *Free Space Optical Communication*, Springer (2017).
52. A. Ghasemi, A. Abedi, and F. Ghasemi, *Terrestrial Mobile Radio Propagation*, pp. 215–287, Springer, New York (2012).
53. M. A. Esmail, H. Fathallah, and M.-S. Alouini, "An experimental study of FSO link performance in desert environment," *IEEE Commun. Lett.* **20**(9), 1888–1891 (2016).

Pierre Didier received his dual MSc degrees in engineering from Grenoble INP-Phelma, Grenoble, France, and in photonics from Université Grenoble Alpes, Grenoble. He is currently working toward a PhD with Prof. Grillot's group at Télécom Paris, Palaiseau, France, with a focus on deploying free-space chaotic cryptography systems based on quantum cascade lasers and detectors. He was a research intern with Kungliga Tekniska Högskolan, Stockholm, Sweden, where he worked on X-ray photon detection using single photon semiconductor detectors. He then was with Thales Research Laboratory, Palaiseau, France, working on midinfrared fiber lasers. His research interests include midinfrared photonics, semiconductor components, and communication systems.

Thomas Bonazzi received his MSc degrees in engineering from ESPCI, France and in fundamental physics and condensed matter from ENS, France, and is now working toward a PhD at LPENS in Prof. Sirtori's group with Prof. Vasanelli, working on high-speed mid-infrared optoelectronic devices with III-V semiconductors and focusing on the development of detectors and modulators for free space optical transmissions.

Olivier Spitz received his PhD in electrical engineering from Université Paris-Saclay, Saclay, France, in 2019, and was awarded the Springer-Nature outstanding thesis prize as well as the Délégation Générale de l'Armement (DGA) thesis prize for his work on the nonlinear dynamics of quantum cascade lasers under external optical feedback/injection. His work on private communication with chaotic quantum cascade lasers was one of the 30 featured discoveries in the 2021 OPN's Year in Optics. He is now a postdoctoral researcher at the University of Central Florida, Orlando, Florida.

Elie Awwad joined Télécom Paris in October 2019 as an assistant professor (Maître de Conférences) in the optical transmission team. His current research deals with mitigation of nonlinear effects in fiber optic communications, margin reductions in optical networks, and optical fiber sensing. He holds a PhD in communications and electronics from Télécom Paris (2015). He worked as a research scientist at Nokia (formerly Alcatel-Lucent) Bell Labs from 2015 until 2019.

Carlo Sirtori received his PhD in physics from the University of Milan in 1990. The same year he joined Bell Labs, where he started his research career in quantum devices. At Bell Labs, he was one of the inventors of the Quantum Cascade Laser. In 1997, he joined THALES Research & Technology (TRT) in France and soon after became the head of the Semiconductor Laser Group. He was appointed full professor at the University of Paris Diderot in 2003 and in 2018 moved to the École Normale Supérieure as professor/chair at ENS-THALES. He is the author of over 280 articles and has given some 150 invited talks at international conferences. He has received several prestigious awards, such as the Fresnel Prize (European Physical Society) or the "Quantum Devices Award." In 2010, he was also awarded an ERC Advanced Grant for his pioneering research on light–matter interaction.

Frédéric Grillot is currently a full professor at Télécom Paris (France) and a research professor at the University of New Mexico. His current research interests include, but are not limited to, advanced quantum confined devices using III-V compound semiconductors, quantum dots/dashes, light-emitters based on intersubband transitions, non-classical light, nonlinear dynamics, and optical chaos in semiconductor laser systems as well as microwave and silicon photonics applications. He strongly contributes to promoting and supporting the development of the general optics community. He has published over 130 journal articles, three book chapters, and many contributions in major international conferences and workshops. He is also a Fellow Member of SPIE, as well as a senior member of the IEEE Photonics Society and of Optica, where he also serves as deputy editor of *Optics Express*. In 2022, he received the IEEE Photonics Society Distinguished Lecturer Award, which is designed to honor excellent speakers who have made technical, industrial, or entrepreneurial contributions to the field of photonics.

Biographies of the other authors are not available.